Catalysis Today 175 (2011) 585–592

Contents lists available at ScienceDirect

Catalysis Today

journal homepage: www.elsevier.com/locate/cattod

Novel nanosized $Ce_xZr_{1-x}O_2$, $Ce_xHf_{1-x}O_2$ and $Ce_xTb_{1-x}O_{2-\delta}$ solid solutions: Structural characteristics and catalytic performance

Benjaram M. Reddy*, Lakshmi Katta, Gode Thrimurthulu

Inorganic and Physical Chemistry Division, Indian Institute of Chemical Technology, Uppal Road, Hyderabad 500 607, India

ARTICLE INFO

Article history:
Received 23 October 2010
Received in revised form 2 February 2011
Accepted 28 February 2011
Available online 2 April 2011

Keywords:
Solid solutions
Coprecipitation
Structural characterization
Oxygen storage capacity (OSC)

ABSTRACT

Nanosized ceria–zirconia, ceria–hafnia and ceria–terbia solid solutions were synthesized by a modified coprecipitation method and evaluated for oxygen storage/release capacity (OSC) and CO oxidation activity. The physicochemical characteristics were investigated by various techniques namely, XRD, Raman, XPS, ISS, UV–vis DRS, TEM and BET surface area. XRD and Raman results revealed formation of $Ce_{0.75}Zr_{0.25}O_2$, $Ce_{0.8}Hf_{0.2}O_2$ and $Ce_{0.8}Tb_{0.2}O_{2-\delta}$ solid solutions typical of fluorite like cubic structure. Variation in the lattice parameter confirmed the successful incorporation of dopant cations into the ceria lattice. XPS measurements revealed that Ce is present in both 3+ and 4+ oxidation states in all samples. UV–vis DRS studies suggested the presence of $Ce^{3+} \leftarrow O^{2-}$ charge transfer transitions attributed to oxygen defects in all the samples. ISS measurements indicated surface enrichment of cerium in ceria–hafnia solid solutions. The ceria–hafnia solid solutions exhibited a high OSC and better CO oxidation activity among the investigated samples. Systematic investigation of these materials provided valid information about the key factors that control the catalytic efficiency of the solid solutions for OSC and CO oxidation.

1. Introduction

The three-way-catalytic (TWC) technology is an indispensable for de-pollution processes in auto-exhaust system of ubiquitous automobiles which can effectively oxidize the harmful CO and hydrocarbons (HC), and reduce NO_x to safer gasses [1–3]. However, fuel rich or oxygen lean and fuel lean or oxygen rich conditions result in low conversion of CO and NO_x, respectively. Hence, to enlarge the air-fuel (A/F) window, ceria (CeO_2) has been used as an active promoter for few decades due to its ability to store/release oxygen which is primarily caused by the fluorite crystal structure that it adopts and the low redox potential among the two valence states (3+ and 4+) [4,5]. Thus, CeO_2 has been a crucial material in the TWC technology and the role of ceria can be very diverse, besides, many technological and bio-applications are also benefited based on its unique properties of oxygen storage capacity (OSC) and $Ce^{3+} \leftrightarrow Ce^{4+}$ redox ability [6,7]. In spite of these advantages, under high thermal and long term annealing conditions the beneficial characteristics of ceria will obviously be affected [8–10]. Another problem associated with the TWC applications is the cold start period at which the pollutant emissions cannot be effectively converted. Therefore, characteristics of ceria must be improved to meet high efficiency in the broad range of temperatures as the TWCs are required to work under low and high thermal conditions as well. Many studies were undertaken in this direction to increase the thermal stability and the OSC properties of ceria.

In particular, doped ceria catalysts have been extensively investigated because of their improved physicochemical properties and decreased oxidation enthalpies compared to pure ceria [11,12]. Additives such as zirconia are known to enhance the activity of ceria by making more oxygen available from the bulk for surface reactions [5]. We have also thoroughly investigated the redox properties and OSC of ceria–zirconia (CZ; $Ce_xZr_{1-x}O_2$) solid solutions [12]. Incorporation of Zr^{4+} into CeO_2 lattice has been proved to enhance the thermal stability and redox characteristics of ceria by forming $Ce_xZr_{1-x}O_2$ solid solutions, and this combination has been extensively employed in the TWC applications [5]. The quest for the present study was to dope ceria with a variable valent cation ($Tb^{3+/4+}$) and an isovalent cation (Hf^{4+}), and compare with the well proven ceria–zirconia solid solutions. As a consequence of doping, the resultant oxygen vacancies and strain in the materials are thought to promote the OSC and CO oxidation activity, thus, suggesting highly promising TWC application prospects for the new $Ce_xTb_{1-x}O_{2-\delta}$ (CT) and $Ce_xHf_{1-x}O_2$ (CH) solid solutions. Apart from cerium, other rare earth elements like terbium also exhibit variable valences. In addition, this element easily acquires the 3+ oxidation state compared to cerium. Therefore, the presence of second redox element besides Ce may also provide additional pathways for the redox reactions at the surface, assisting its catalytic action for CO oxidation. The ionic radius of Hf^{4+} is smaller

* Corresponding author. Tel.: +91 40 27191714; fax: +91 40 2716 0921.
E-mail addresses: bmreddy@iict.res.in, mreddyb@yahoo.com (B.M. Reddy).

0920-5861/$ – see front matter © 2011 Elsevier B.V. All rights reserved.
doi:10.1016/j.cattod.2011.02.047

than Zr^{4+} hence the strain induced by the Hf^{4+} incorporation into the ceria lattice may even influence more than Zr^{4+}, which may lead to enhancement in the oxide ion mobility. In order to understand the properties like oxygen vacancies, OSC and redox characteristics, we have prepared CZ, CT and CH solid solutions by a modified coprecipitation method from ultra high dilute solutions and investigated their structural and redox properties employing powder X-ray diffraction (XRD), transmission electron microscopy (TEM), X-ray photoelectron spectroscopy (XPS), UV–visible diffuse reflectance spectroscopy (UV–vis DRS), Raman spectroscopy (RS), ion scattering spectroscopy (ISS) and BET surface area techniques. The OSC and catalytic activity towards CO oxidation have also been evaluated to correlate with the physicochemical characteristics of the synthesized solid solutions.

2. Experimental

2.1. Preparation of catalysts

The investigated $Ce_xZr_{1-x}O_2$ (CZ, 50:50 mol%), $Ce_xTb_{1-x}O_{2-\delta}$ (CT, 80:20 mol%) and $Ce_xHf_{1-x}O_2$ (CH, 80:20 mol%) solid solutions were prepared by adopting a coprecipitation method using ammonium cerium(IV) nitrate (LobaChemie, GR grade) and zirconium(IV) nitrate (Aldrich, AR grade) or terbium(III) nitrate (Aldrich, AR grade) or hafnium(IV) chloride (Aldrich, AR grade), respectively. The desired amounts of precursors were dissolved separately in double-distilled water under mild stirring conditions and mixed together. Upon complete mixing, an excess aqueous ammonium hydroxide solution was added slowly to the aqueous nitrate mixture solution until the precipitation was complete (pH = ~8.5) and the solid so obtained was washed, filtered and dried in oven during 12 h at 393 K. After grinding the dried product, subsequently calcined at 773 K for 5 h at a heating rate of 5 K min^{-1} in air atmosphere to obtain the final oxide materials. To understand the thermal behaviour, the obtained samples were subjected to additional calcination at 873, 973 and 1073 K for 5 h. After cooling, the solid residues were ground using a ceramic mortar and pestle until the fine powders were obtained, and stored in dry atmosphere. A pure ceria (C) sample was also prepared under identical conditions for the purpose of comparison.

2.2. Catalyst characterization

Powder XRD patterns were collected on a Rigaku Multiflex instrument equipped with nickel-filtered Cu Kα (0.15418 nm) radiation source and a scintillation counter detector. The step size and the time per step were respectively fixed at 0.02° and 1 s in the range of $12^\circ \leq 2\theta \leq 80^\circ$. The XRD phases present in the samples were identified with the help of Powder Diffraction File-International Center for Diffraction Data (PDF-ICDD). The mean crystallite size of solid solution phases was estimated with the help of Scherrer equation by line broadening technique, and the lattice parameter was calculated by a standard cubic indexation method using the intensity of most prominent peaks.

The UV-Raman spectra were obtained at room temperature using a LabRam HR800UV Raman spectrometer (Horiba Jobin-Yvon) fitted with a confocal microscope and liquid-nitrogen cooled charge-coupled device (CCD) detector. Samples were excited with 325 nm of a He–Cd laser (MellesGriot Laser) which is focused on the sample under the microscope with the diameter of the analyzed spot being ~1 μm. The acquisition time was adjusted according to the intensity of Raman scattering. The wavenumber values reported from the spectra are accurate to within 1 cm^{-1}. The BET surface areas were determined by N_2 physisorption at liquid N_2 temperature on a Micromeritics Gemini 2360 instrument. Prior to analysis, the samples were oven dried at 393 K for 12 h and flushed with Argon gas for 2 h. The UV–vis DRS measurements were performed over the wavelength range of 200–750 nm using a GBS-Cintra 10e UV–vis NIR spectrophotometer with an integration sphere diffuse reflectance attachment. Samples were diluted in KBr matrix by pelletization.

The TEM-HREM studies were made on a JEM-2010 (JEOL) instrument equipped with a slow-scan CCD camera and at an accelerating voltage of 200 kV. Samples for TEM analysis were prepared by crushing the materials in an agate mortar and dispersing ultrasonically in ethyl alcohol. After well dispersion, a droplet was deposited on a copper grid supporting a perforated carbon film and allowed to dry. The specimen was examined under vacuum at room temperature.

XPS analyses were performed using a Shimadzu (ESCA 3400) spectrometer. The X-ray source utilized was Mg Kα (1253.6 eV) radiation. The analysis was done at room temperature and pressures were typically on the order of less than 10^{-8} Pa. The samples were out gassed overnight in a vacuum oven at 283 K before XPS measurements. All binding energies were measured within a precision of ±0.3 eV.

IS spectra were measured on a Leybold surface analysis system equipped with X-ray and ion sources and an EA 10/100 electron (ion) analyzer with multichannel detection (Specs). Samples were activated in flowing synthetic air (20% O_2/N_2) at 573 K for 30 min before they were introduced into the spectrometer vacuum without further contact with the ambient humid atmosphere (in situ treatment). The measurements were made with 3000 eV Ar^+ ions and recorded with the analyzer in pass-energy mode (pass energy 84.5 eV). The surface charge was removed with a flood gun. The source and the flood gun were allowed to stabilize with the sample withdrawn from the measurement position. Signal intensities were estimated assuming the background to be linear.

The OSC of the catalysts was obtained using a thermogravimetry (TG) method by employing a commercial Netzsch TG–DTA (Luxx, STA, 409 PC, Germany) analyzer under repeated thermal treatments in the temperature window 573–1073 K. The OSC of the catalyst was measured in terms of the amount of oxygen released during cyclic heat treatments. The weight change during the thermal treatments was monitored by TG in flowing nitrogen or dry air. The heat cycle consisted of heating the sample to 1073 K, cooling to 423 K, and again heating to 1073 K. All heating and cooling rates were in the steps of 5 K min^{-1}. The weight loss of the sample during the second stage of heat treatment was used to measure the oxygen release properties.

2.3. CO oxidation reaction

The catalytic activity for oxidation of CO was conducted at normal atmospheric pressure in a fixed-bed microreactor under the temperature ramp of 5 K min^{-1}. Approximately 100 mg catalyst sample (250–355 μm sieve fraction) was diluted with quartz particles (1:1) of the same sieve fraction and placed in a 2 mm i.d., 6 mm o.d., and 250 mm long quartz reactor for the reaction. The temperature was measured using a thermocouple placed near the catalyst bed. The following gasses and gas mixtures were used (supplied by Air Liquide): argon (>99.999% purity), 9.98% CO in argon (CO purity, >99.997% and argon purity, >99.99%) and 10.2% O_2 in argon (oxygen purity, >99.995%). The total flow rates maintained by three mass flow controllers were in the range of 50–60 N mL min^{-1} (millilitres normalized to 273.15 K and 1 atm.). The CO and CO_2 gas concentrations were measured using an Uras 14 infrared analyzer module, and the O_2 concentration was measured using a Magnos 16 analyzer (Hartmann & Braun). Prior to oxidation of CO, catalysts were heated to 773 K in 10.2% O_2/Ar gas mixture, using a heating ramp of 10 K min^{-1}, and kept at the final temperature for 1 h. The oxi-

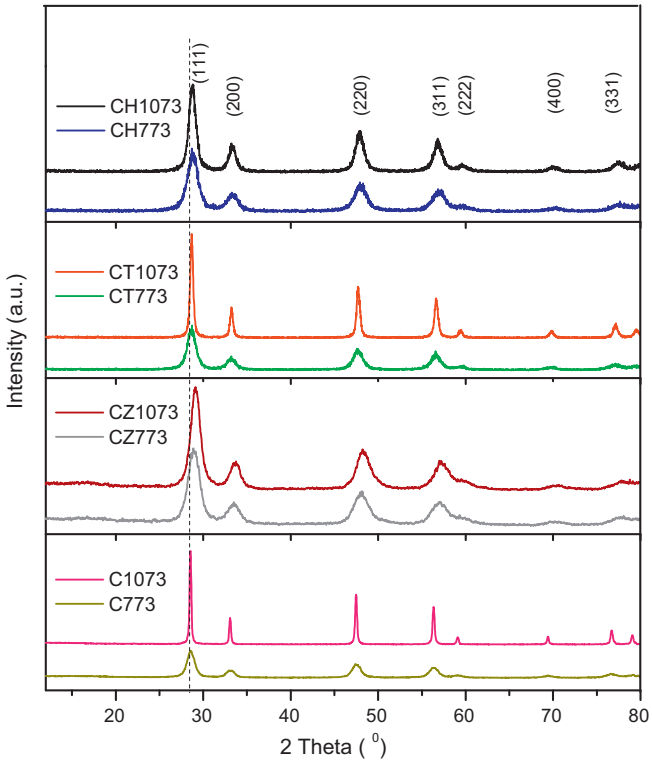

Fig. 1. Powder XRD patterns of CeO_2 (C), $Ce_xZr_{1-x}O_2$ (CZ), $Ce_xTb_{1-x}O_{2-\delta}$ (CT) and $Ce_xHf_{1-x}O_2$ (CH) samples calcined at 773 and 1073 K.

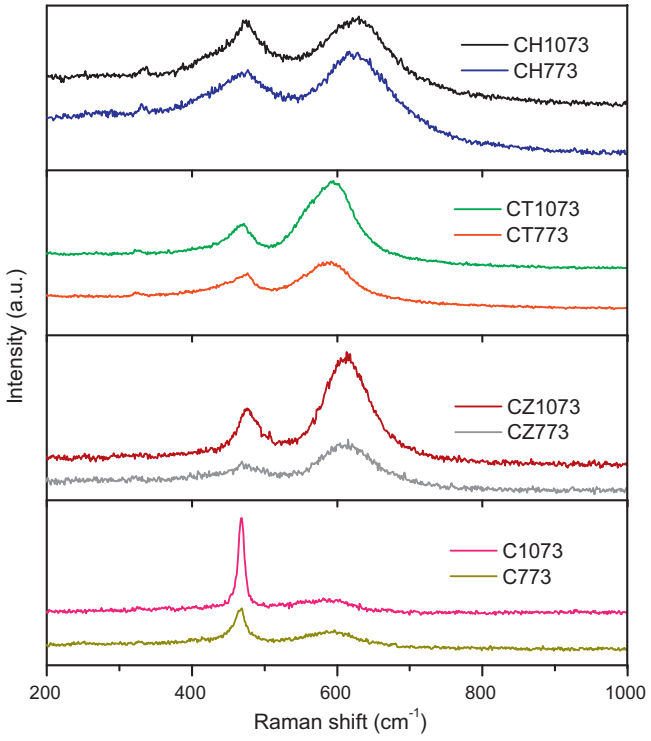

Fig. 2. Raman spectra of CeO_2 (C), $Ce_xZr_{1-x}O_2$ (CZ), $Ce_xTb_{1-x}O_{2-\delta}$ (CT) and $Ce_xHf_{1-x}O_2$ (CH) samples calcined at 773 and 1073 K.

dized sample was then purged in argon. The CO/O_2 reactant feed ratio was 1, and partial pressures of CO and O_2 were in the range of 10 mbar.

3. Results and discussion

3.1. Catalyst characterization

X-ray diffraction patterns of CZ, CT and CH samples calcined at various temperatures are presented in Fig. 1. For comparison, pure ceria XRD profiles are also included in the figure. It is noted from Fig. 1 that all the observed peaks are characteristic of typical cubic fluorite phases. It is also clear from the figure that the peak positions for doped samples, relative to pure ceria, are shifted to higher Braggs angles, and no diffraction peaks pertaining to the individual oxides namely, ZrO_2, HfO_2 and TbO_2 are found indicating the formation of solid solutions with the composition $Ce_{0.75}Zr_{0.25}O_2$ (PDF-ICDD 38-1439), $Ce_{0.8}Tb_{0.2}O_{2-\delta}$ [13] and $Ce_{0.8}Hf_{0.2}O_2$ (PDF-ICDD 04-006-1933) for 773 K calcined samples [12,14]. The lattice parameters of all samples along with pure ceria are calculated using the first four intense peak positions (1 1 1), (2 0 0), (2 2 0) and (3 1 1). The average values with standard deviations are given in Table 1, and the results agree quite well with the values reported in the literature [13–15]. From the lattice parameter values, it is obvious that there is a lattice cell shrinkage due to incorporation of smaller sized Zr^{4+} and Hf^{4+}cations (0.84 and 0.83 Å respectively for Zr^{4+} and Hf^{4+}) into the ceria lattice. On the other hand, the ionic radius of Tb^{3+} (1.04 Å) is higher than the Ce^{4+} therefore little expansion is expected with its introduction. In fact, the lattice expansion is counteracted by the presence of Tb^{4+} (0.88 Å). All these observations provide further evidence for the formation of solid solutions. The diffraction peaks of all samples are lower in intensity and broader than the pure ceria, which implies that the samples are in smaller crystallite size. The crystallite sizes of 773 and 1073 K calcined samples calculated by means of Scherrer equation are shown in Table 1. Upon increasing calcination temperature a gradual sharpening of the peaks is observed in the XRD patterns, revealing an increase in the crystallite size. The XRD patterns of CZ indicated that the sample underwent a phase separation with increase of calcination temperature as confirmed

Table 1
BET surface area, average crystallite size, cell parameter and OSC of CeO_2 (C), $Ce_xZr_{1-x}O_2$ (CZ), $Ce_xTb_{1-x}O_{2-\delta}$ (CT) and $Ce_xHf_{1-x}O_2$ (CH) mixed oxides calcined at 773 and 1073 K.

Sample	BET S.A. ($m^2\ g^{-1}$)	Crystallite size (nm)[a]	Lattice parameter (Å)[a]	OSC (δ)
C 773	41	7.3	5.415 ± 0.004	0.04
C 1073	8	32.5	5.411 ± 0.003	–
CZ 773	84	4.7	5.354 ± 0.003	0.16
CZ 1073	36	5.5	5.274 ± 0.013	–
CT 773	85	5.5	5.405 ± 0.003	0.18
CT 1073	37	12.1	5.395 ± 0.002	–
CH 773	78	4.6	5.338 ± 0.007	0.19
CH 1073	26	13.1	5.334 ± 0.002	–

[a] From the XRD data.

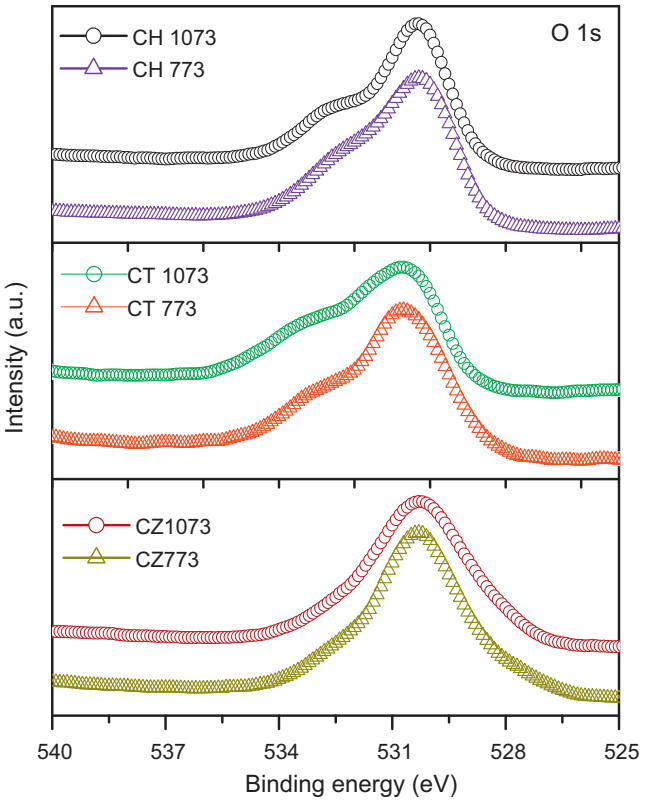

Fig. 3. O 1s XPS patterns of $Ce_xZr_{1-x}O_2$ (CZ), $Ce_xTb_{1-x}O_{2-\delta}$ (CT) and $Ce_xHf_{1-x}O_2$ (CH) samples calcined at 773 and 1073 K.

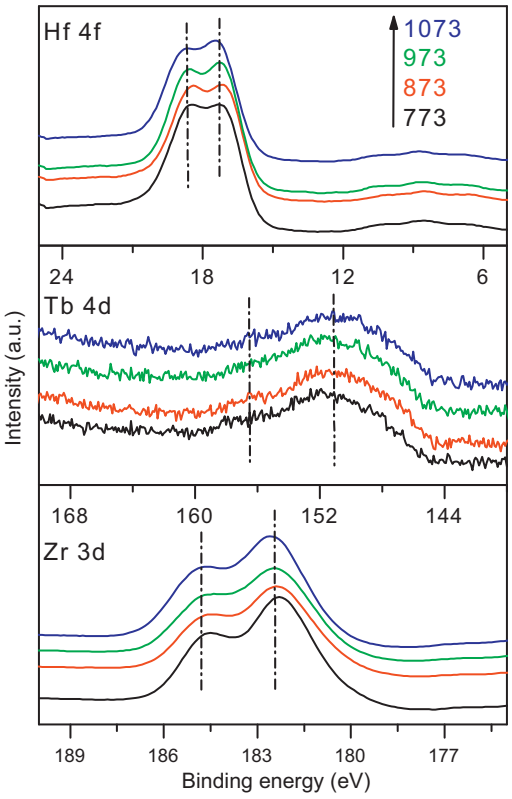

Fig. 5. Zr 3d XPS patterns of $Ce_xZr_{1-x}O_2$ (CZ), Tb 4d patterns of $Ce_xTb_{1-x}O_{2-\delta}$ (CT) and Hf 4f patterns of $Ce_xHf_{1-x}O_2$ (CH) samples calcined at various temperatures from 773 to 1073 K.

by an essential decrease in the lattice parameter. In contrast, the CT and CH remained in a single phase with fluorite structure which further confirmed by unchanged lattice parameter. Hence, these results suggest that the CT and CH samples are quite stable compared to the CZ in the explored temperature range.

RS is very useful technique to confer the information on the oxygen vacancies of oxide materials, especially for CeO_2 containing solid solutions. Raman spectra of various samples are compiled in Fig. 2. The strong band generally observed at ~465 cm^{-1} is typical of fluorite like cubic structure, which can be viewed as symmetric breathing mode of oxygen ions surrounded by the cations [16,17].

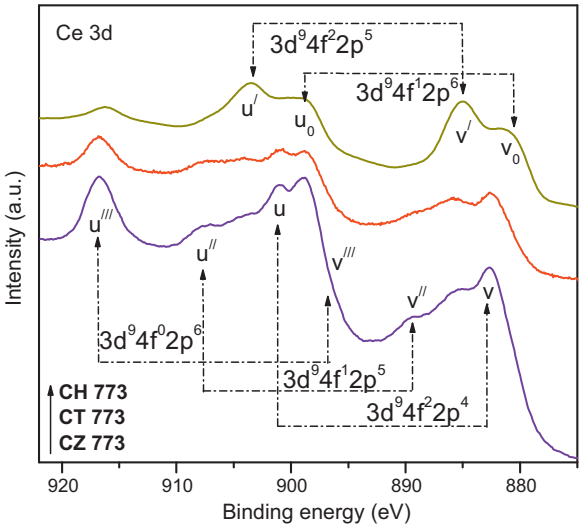

Fig. 4. Ce 3d XPS patterns of $Ce_xZr_{1-x}O_2$ (CZ), $Ce_xTb_{1-x}O_{2-\delta}$ (CT) and $Ce_xHf_{1-x}O_2$ (CH) samples calcined at 773 K.

The peak at 465 cm^{-1} progressively shifts to higher wavenumbers, broadens, and becomes asymmetric when the ceria particle size gets smaller. The size dependence has been attributed to the inhomogeneous strain broadening associated with dispersion in particle

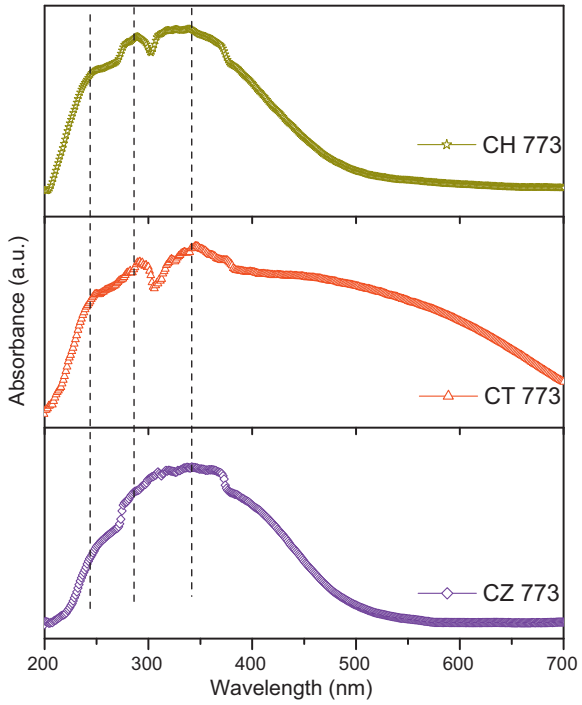

Fig. 6. UV–vis DRS of $Ce_xZr_{1-x}O_2$ (CZ), $Ce_xTb_{1-x}O_{2-\delta}$ (CT) and $Ce_xHf_{1-x}O_2$ (CH) samples calcined at 773 K.

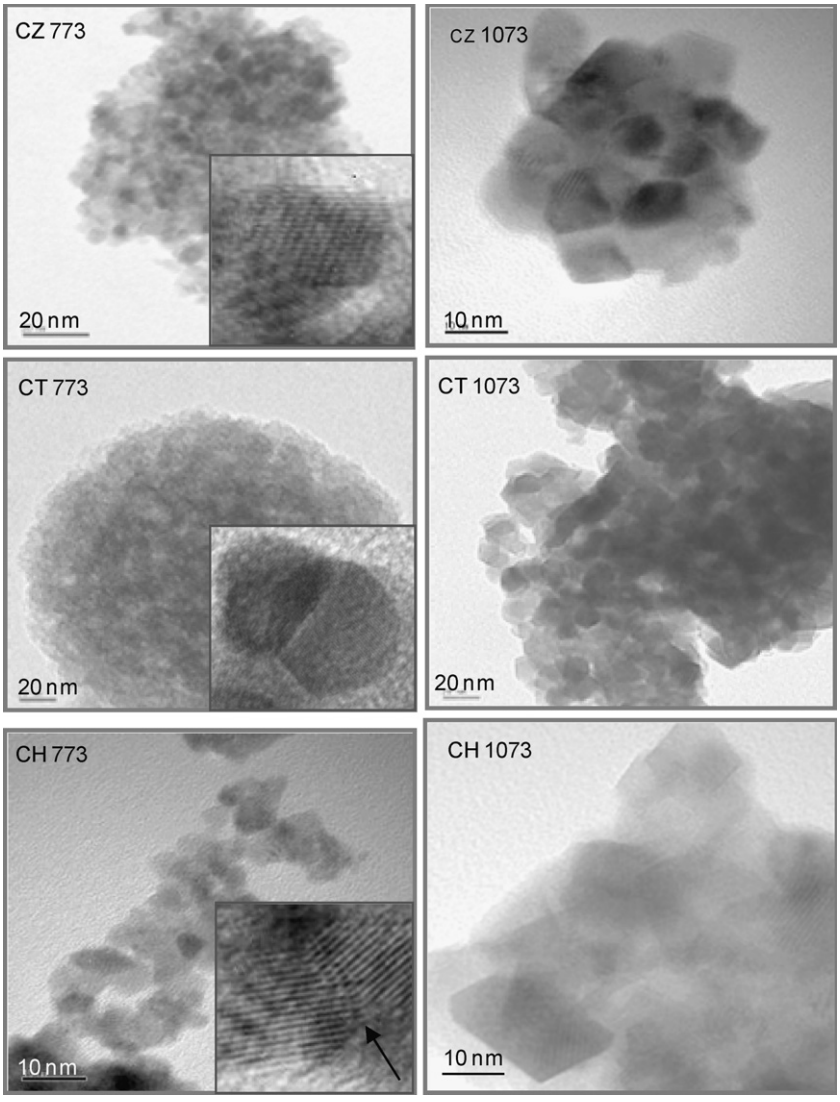

Fig. 7. Representative TEM images of $Ce_xZr_{1-x}O_2$ (CZ), $Ce_xTb_{1-x}O_{2-\delta}$ (CT) and $Ce_xHf_{1-x}O_2$ (CH) sample calcined at 773 and 1073 K.

size and phonon confinement [18]. The shift in the F_{2g} mode is also attributed to change in the M–O vibration for doped ceria which account for the difference in the ionic radius of the dopant ion. As envisaged earlier, the small sized dopant ions incorporation enable changes in the lattice parameter owing to cell contraction [12,19]. Vibrations are rapid for contracted lattice so that band shifts to higher wavenumbers. In addition, the full width at half maximum increased compared to pure ceria which is inline with XRD results. Along with this band one more intense band at $\sim$590 cm^{-1} is also noted assigned to non-degenerate Longitudinal Optical (LO) mode arising due to relaxation of symmetry rules, which is attributed to charge compensating defects induced by the incorporation of other metal cations into the ceria lattice [20,21]. The substitution of Ce ion leading to the formation of oxygen vacancies is known to be responsible for the emergence of this band. The strong enhancement of this band under UV excitation is due to the multiphonon excitation by resonance Raman effect [18,22]. Generally, this effect is often observed when the excitation energy is comparable to the band gap energy and is sensitive to the defect formation in ceria and doped ceria materials. Particularly, for CH sample the intensity of this band is high in association with more number of oxygen vacancies present in the sample. The F_{2g} peak intensity is greatly influenced by the calcination temperature [18]. As noted from the figure, with increasing calcination temperature the intensity of the F_{2g} band increased owing to better crystallization.

The XPS study was performed on various samples calcined at different temperatures and the results are shown in Figs. 3–5 corresponding to O 1s, Ce 3d and Zr 3d, Tb 4d and Hf 4f, respectively. The O 1s core level spectra of various samples are presented in Fig. 3. The O 1s spectra are mainly composed of two components. The low energy peak observed at ca. 530.3 ± 0.3 eV corresponds to lattice oxygen. In addition to the main peak, an apparent shoulder peak at higher binding energy 533.0 ± 0.3 eV is due to surface hydroxyls and carbonate groups [23]. The hydroxyl groups are generally associated with the Ce^{3+} ions that are located on the surface, therefore the one with high intense shoulder at this region is with more number of Ce^{3+} ions. From Fig. 3, it is evident that as we go from Zr → Tb → Hf, the high energy peak becomes more significant and the corresponding mixed oxide is more reducible. With an increase in the calcination temperature, the intensity of this shoulder peak decreased which could be due to removal of the surface residues. The Ce 3d core level spectra of various samples are presented in Fig. 4. The Ce 3d spectrum is composed of five spin orbit doublets due to two multiplets, 3/2 (u) and 5/2 (v) [24,25]. These ten peaks are usually labeled as v^0, v, v', v" and v"' and u^0, u, u', u" and u"' respectively in the literature. Here, v/u, v″/u″ and

v‴/u‴ are attributed to Ce^{4+}; v/u and v″/u″ that are due to a mixture of $3d^94f^2O2p^4$ and $3d^94f^1O2p^5$ configurations, and v‴/u‴ is a $3d^94f^0O2p^6$ final state. While, v^0/u^0 and v′/u′ are due to $3d^94f^1O2p^6$ and $3d^94f^2O2p^5$ corresponding to Ce^{3+} [26]. It is observed that the intensity of u‴ decreases from Zr → Tb → Hf with a simultaneous increase in the v′ intensity. Therefore, the conversion from $Ce^{4+} \rightarrow Ce^{3+}$ and thus relative amount of Ce^{3+} is enhanced in the same order in association with oxygen mobility.

The Zr 3d, Tb 4d and Hf 4f core level spectra are presented in Fig. 5. The slightly resolved peaks at about 184.6 and 182.2 eV for Zr 3d of CZ samples correspond to the Zr $3d_{3/2}$ and Zr $3d_{5/2}$, respectively, which agrees well with the values reported in the literature for Zr(IV)O_2 [27,28]. The splitting energy between the Zr $3d_{3/2}$ and Zr $3d_{5/2}$ photoemission feature is ~2.4 eV, which is in agreement with the earlier reports [29]. From the Tb 4d XPS core level spectra, multi-oxidations of Tb can be understood. The pronounced shoulder at below 150 eV, a maximum at 151.7 eV, and tailing towards 160 eV shows the presence of more than one oxidation state i.e., 3+ and 4+, respectively. The lattice parameter from XRD of CT is also supported the presence of Tb in both 3+ and 4+ oxidation states. With increase in the calcination temperature, the low energy shoulder is decreased slightly, indicating a little higher Tb^{4+}contribution under high calcination temperature. The slightly elevated features at about 17.2 and 18.6 eV observed for CH samples are respectively representative to the Hf $4f_{7/2}$ and Hf $4f_{5/2}$. The binding energy difference in between these two components is about 1.4 eV which is inline with the earlier reported values [28]. From the Hf 4f XP spectra, it is observed that Hf is mainly in 4+ oxidation state [28].

UV–vis DRS technique is effectively used for the study of metal oxides to obtain information about the charge transfer transitions. Ceria exhibits strong absorption below 400 nm caused by charge transfer bands. DR spectra of CZ, CT and CH samples calcined at 773 K are presented in Fig. 6. Three characteristic bands of ceria corresponding to the $O^{2-} \rightarrow Ce^{4+}$ and $O^{2-} \rightarrow Ce^{3+}$ charge transfer bands and inter-band transitions in the wavelength range 250–340 nm are observed for all samples [17]. The occurrence of oxygen vacancy defects noticed from Raman spectroscopy studies supports the $O^{2-} \rightarrow Ce^{3+}$ transitions, which are more prominent and comparatively well resolved for CH sample than the other mixed oxides. These observations are in line with the v′ peak intensity of the Ce 3d core level XP spectra. The absorption edge of doped ceria samples shifted towards lower wavelengths (quantum confinement effect) relative to pure ceria due to decrease in the crystallite size [17].

The specific surface areas of all the samples calcined at 773 and 1073 K are shown in Table 1. A systematic decline in the surface area is observed with increase in the calcination temperature. Higher calcination temperatures can cause sintering and growth of the particles which result in the gradual decrease of the surface area. However, the thermal resistance to sintering of the solid solutions is improved when compared to pure ceria. The OSC values of various samples measured by thermogravimetry method are presented in Table 1. It is reported earlier that the OSC of the sample is influenced by many factors including surface area, crystallite size, method of preparation, homogeneity and so on. However, it is interesting to note that the sample with low specific surface area (CH) is showing high OSC than the other two mixed oxides (CZ and CT). This indicates that along with surface oxygen, oxygen from the bulk is also participating in the exchange process and contributes to the oxygen storage [14]. This could be due to Hf^{4+} enrichment in the bulk (discussed in ensuing section) which facilitates bulk oxygen mobility. In fact, the Zr and Hf isovalent ions have shown small difference in the ionic radius, nevertheless, the other factors also such as strain, oxygen diffusion, phase domains, grain boundary, and/or texture effects play an important role in the overall oxygen storage process. Moreover, as reported earlier, the oxygen vacancies are trapped by the Zr cation in CZ with consequent decrease

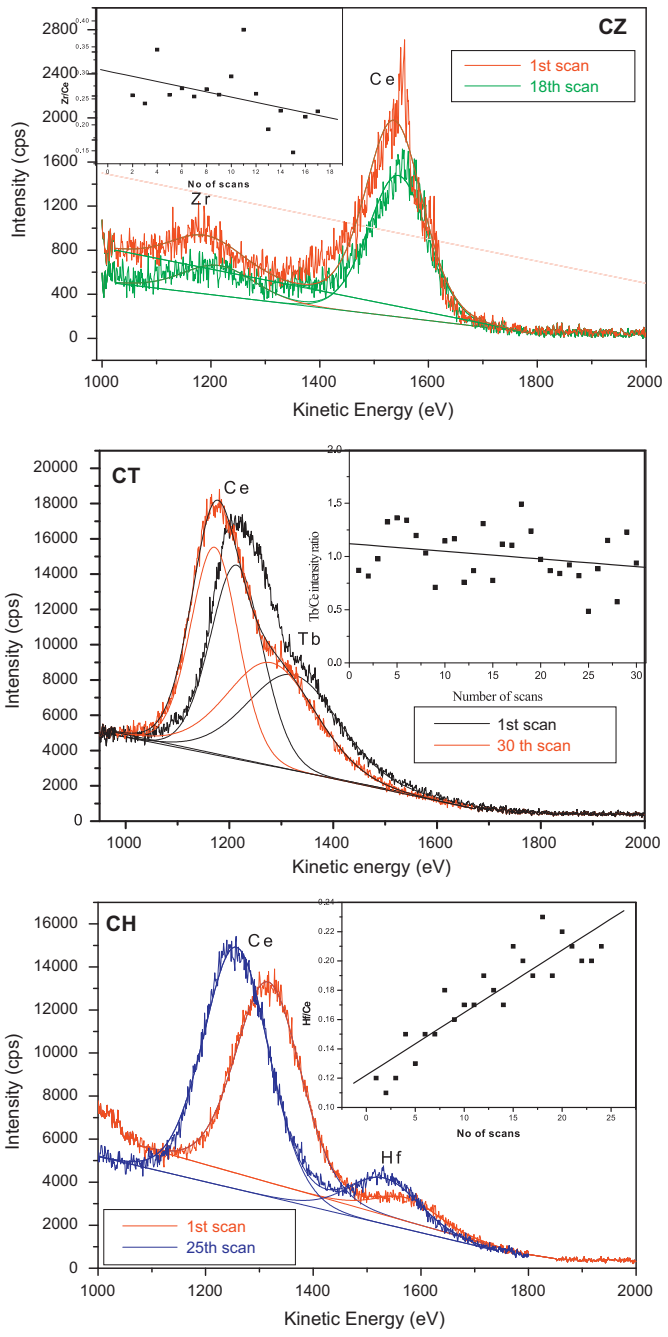

Fig. 8. ISS patterns of $Ce_xZr_{1-x}O_2$ (CZ) after 1st and 18th scan (inset: Zr/Ce versus number of scans), $Ce_xTb_{1-x}O_{2-\delta}$ (CT) after 1st and 30th scan (inset: Tb/Ce versus number of scans) and $Ce_xHf_{1-x}O_2$ (CH) after 1st and 25th scan (inset: Hf/Ce versus number of scans) samples calcined at 773 K.

in the oxygen diffusion and hence oxygen storage due to its slight high electro negativity [15]. Therefore, CH sample has shown high OSC when compared to CZ. In the case of CT sample, presence of Tb^{3+} enhances the OSC by creating oxygen vacancies via charge compensation mechanism.

The morphology of the samples could be known by the investigation with transmission electron microscopy. The representative TEM pictures of CZ, CT and CH samples calcined at 773 and 1073 K are presented in Fig. 7. The TEM pictures revealed that all samples are ensemble of nanosized particles which are distributed uniformly and bear a fluorite like cubic structure. The average particle size of 773 K calcined samples is 5–6 nm and it is observed that the particles are aggregated with increase in the calcination tem-

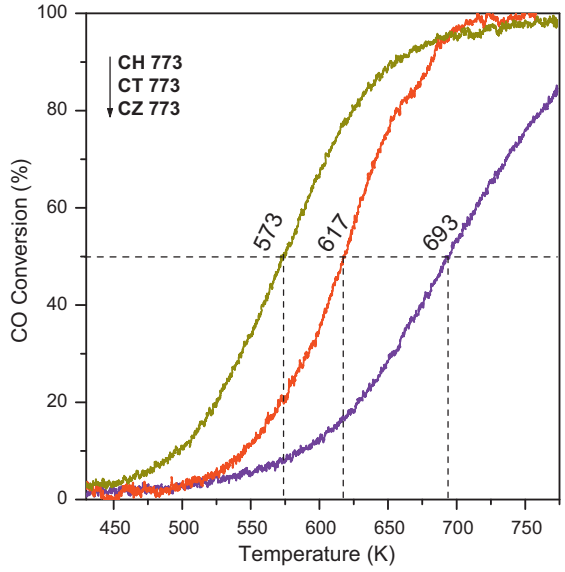

Fig. 9. Conversion of CO over $Ce_xZr_{1-x}O_2$ (CZ), $Ce_xTb_{1-x}O_{2-\delta}$ (CT) and $Ce_xHf_{1-x}O_2$ (CH) samples calcined at 773 K as a function of reaction temperature (down arrow indicates the increasing order of T_{50} temperature).

perature, and the results are consistent with those calculated by Scherrer equation based on XRD line broadening. From the figures, few overlapping regions are also observed and these overlapped regions are known to act as active sites for the adsorption of the gaseous CO and O_2 and further facilitate the oxidation reaction. The enlarged regions are incorporated as insets in the figure.

The ISS intensity (cps) versus kinetic energy (eV) plots of the CZ, CT and CH samples (773 K calcined) after definite scans are presented in Fig. 8a–c, respectively. The insets show the intensity ratios between Zr and Ce, Tb and Ce, and Hf and Ce, respectively. It can be observed from the figure that there is a linear increase in the Hf/Ce intensity ratio during the sputter series, i.e., the Ce is enriched at the external surface of the mixed oxide. In case of CZ and CT samples, such strong surface enrichment is not detected. Upon extended sputtering of the surface there is a slight decrease in the Zr/Ce intensity ratio and no trend is observed in the Tb/Ce intensity ratio. The surface enrichment of Ce in CH sample may be responsible for the observed high reducibility over the other two mixed oxides at relatively low temperatures.

3.2. Catalyst activity

The CO oxidation occurs via Mars-van Krevelen redox type mechanism. In the absence of oxygen, CO gets oxidized by consuming lattice oxygen and leaving the oxygen vacancy. In the presence of oxygen, the dissociative chemisorption of dioxygen replenishes the surface vacancies [30]. The evaluation of CO oxidation has been carried out to understand the effect of isovalent (Hf^{4+}) cation and variable valent cation ($Tb^{3+/4+}$) substitution in the ceria lattice. The catalytic activities of various samples calcined at 773 K for CO oxidation in the temperature range from 430 to 775 K are presented in Fig. 9. For CH sample, the reaction is underway at below 470 K temperature and increased the conversion drastically, whereas, for CT and CZ samples, the reaction starts at above 540 K temperature and increased modestly. We have evaluated the light off curves (T_{50} – the temperature at 50% conversion of CO) to better understand the catalytic activity. Among all the samples, CH sample exhibited low T_{50} and high CO conversions over CT and CZ. The light-off temperatures of CH, CT and CZ are 573, 617 and 693 K, respectively. The catalytic activity of various samples is in the following order: CH 773 > CT 773 > CZ 773 as their light off temperatures are in the reverse order. The high activity of CH is attributed to high oxygen storage and its mobility. The significant enhancement in the catalytic activity of CH sample is also correlated with decrease in u‴ with simultaneous increase in v′ peak intensity of the Ce 3d XPS core level spectra, a pronounced high energy shoulder for O 1s core level spectra, more oxygen vacancies from UV-RS and well resolved and prominent UV–vis DRS $Ce^{3+} \leftarrow O^{2-}$ charge transfer band. Slight Ce surface enrichment in the ISS studies is also responsible for high CO catalytic activity of the CH sample due to which active sites could be increased on the surface to absorb more amount of CO and offer better activity at relatively lower temperatures. In the case of CT sample, the high CO conversion could be ascribed to more amount of weakly held oxygen which certainly contributes to CO conversion [31].

4. Conclusions

The Zr, Tb and Hf incorporated ceria samples were synthesized selectively via a modified coprecipitation method using aqueous NH_3 solution as the precipitating agent. All samples exhibited fluorite like cubic structure with thermally stable ultrafine nanoparticles of 5–10 nm range and exhibited high specific surface area in the range of 78–85 $m^2\,g^{-1}$. Raman results disclosed the presence of more number of oxygen vacancies in the samples. The oxidation state of Ce has been determined by XPS. In the CT sample, the Tb is present in both 3+ and 4+ oxidation states as revealed by XPS. Relatively high amount of Ce^{3+} is observed in CH sample from the Ce 3d core level XP spectra. A well-resolved $Ce^{3+} \leftarrow O^{2-}$ band is observed for CH sample compared to CZ and CT samples. ISS results revealed a slight surface enrichment of Ce on the CH surface. CH sample exhibited a high OSC among the investigated ceria-based mixed oxides. The high stability under thermal treatments and a high CO conversion at relatively lower temperatures makes the CH solid solution as a promising material for oxygen storage/release processes and automotive three-way-catalytic applications.

Acknowledgements

We greatly acknowledge Prof. Dr. W. Grünert, RUB, Germany for providing ISS and CO oxidation results. We also thank Dr. Tetsuo Umegaki, AIST-Kansai, Japan for help in XPS measurements. L.K. and G.T. wish to thank the Council of Scientific and Industrial Research (CSIR), New Delhi for senior research fellowships. Financial support was received from Department of Science and Technology, New Delhi, under SERC Scheme (SR/S1/PC-63/2008).

References

[1] M.F. Garcia, A.M. Arias, J.C. Hanson, J.A. Rodriguez, Chem. Rev. 104 (2004) 4063–4103.
[2] H. Zhu, Z. Qin, W. Shan, W. Shen, J. Wang, J. Catal. 225 (2004) 267–277.
[3] A.I. Juez, A.M. Arias, M.F. García, J. Catal. 221 (2004) 148–161.
[4] R. Wang, P.A. Crozier, R. Sharma, J.B. Adams, Nano Letters 8 (2008) 962–967.
[5] M. Sugiura, Catal. Surv. Asia 7 (2003) 77–87.
[6] X. Liu, K. Zhou, L. Wang, B. Wang, Y. Li, J. Am. Chem. Soc. 131 (2009) 3140–3141.
[7] A. Trovarelli, Catal. Rev. Sci. Eng. 38 (1996) 439–520.
[8] F. Giordano, A. Trovarelli, C. de Leitenburg, G. Dolcetti, M. Giona, Ind. Eng. Chem. Res. 40 (2001) 4828–4835.
[9] E. Mamontov, T. Egami, R. Brezny, M. Koranne, S. Tyagi, J. Phys. Chem. B 104 (2000) 11110–11116.
[10] J. Mikulova, S. Rossignol, J. Barbier Jr., D. Duprez, C. Kappenstein, Catal. Today 124 (2007) 185–190.
[11] H. Li, L. Zhang, H. Dai, H. He, Inorg. Chem. 48 (2009) 4421–4434.
[12] B.M. Reddy, P. Bharali, P. Saikia, A. Khan, S. Loridant, M. Muhler, W. Grünert, J. Phys. Chem. C 111 (2007) 1878–1881.
[13] B.M. Reddy, P. Saikia, P. Bharali, Y. Yamada, T. Kobayashi, M. Muhler, W. Grünert, J. Phys. Chem. C 112 (2008) 16393–16399.
[14] B.M. Reddy, P. Bharali, P. Saikia, S.-E. Park, M.W.E. van den Berg, M. Muhler, W. Grünert, J. Phys. Chem. C 112 (2008) 11729–11737.
[15] G. Balducci, M.S. Islam, J. Kašpar, P. Fornasiero, M. Graziani, Chem. Mater. 12 (2000) 677–681.

[16] V.S. Escribano, E.F. Lopez, M. Panizza, C. Resini, J.M.G. Amores, G. Busca, Solid State Sci. 5 (2003) 1369–1376.
[17] B.M. Reddy, L. Katta, G. Thrimurthulu, Chem. Mater. 22 (2010) 467–475.
[18] T. Taniguchi, T. Watanabe, N. Sugiyama, A.K. Subramani, H. Wagata, N. Matsushita, M. Yoshimura, J. Phys. Chem. C 113 (2009) 19789–19793.
[19] J. Xu, P. Li, X. Song, C. He, J. Yu, Y.-F. Han, J. Phys. Chem. Lett. 1 (2010) 1648–1654.
[20] B.M. Reddy, A. Khan, Catal. Surv. Asia 9 (2005) 155–171.
[21] J.R. McBride, K.C. Hass, B.D. Poindexter, W.H. Weber, J. Appl. Phys. 76 (1994) 2435–2441.
[22] Z. Wu, M. Li, J. Howe, H.M. Meyer III, S.H. Overbury, Langmuir 26 (2010) 16595–16606.
[23] Y.-W. Zhang, R. Si, C.-S. Liao, C.-H. Yan, J. Phys. Chem. B 107 (2003) 10159–10167.
[24] F.L. Normand, J.E. Fallah, L. Hilaire, P. Legare, A. Kotani, J.C. Parlebas, Solid State Commun. 71 (1989) 885–889.
[25] D.R. Mullins, S.H. Overbury, D.R. Huntley, Surf. Sci. 409 (1997) 307–319.
[26] P.J. Miedziak, Z.T. Tang, T.E. Devies, D.I. Enache, J.K. Bartley, A.F. Carley, A.A. Herzing, C.J. Kiely, S.H. Taylor, G.J. Hutchings, J. Mater. Chem. 19 (2009) 8619–8627.
[27] Practical surface analysis, in: D. Briggs, M.P. Seah (Eds.), Auger and X-ray Photoelectron Spectroscopy, vol. 1, 2nd ed., Wiley, New York, 1990.
[28] C.D. Wagner, W.M. Riggs, L.E. Davis, J.F. Moulder, in: G.E. Muilenberg (Ed.), Handbook of X-ray Photoelectron Spectroscopy, Perkin-Elmer Corporation, Minnesota, 1978.
[29] S.-P. Wang, X.-C. Zheng, X.-Y. Wang, X.-R. Wang, S.-M. Zhang, L.-H. Yu, W.-P. Huang, S.-H. Wu, Catal. Lett. 105 (2005) 163–168.
[30] A. Eleonora Jr., Llorca, M. Boaro, A. Trovarelli, J. Catal. 234 (2005) 88–95.
[31] G. Zhou, R.J. Gorte, J. Phys. Chem. B 112 (2008) 9869–9875.